IEEE Access
Multidisciplinary | Rapid Review | Open Access Journal

Received July 23, 2017, accepted September 7, 2017, date of publication September 18, 2017, date of current version October 12, 2017.

Digital Object Identifier 10.1109/ACCESS.2017.2753578

Multistatic Millimeter-Wave Imaging by Multiview Portable Camera

JAIME LAVIADA[1], ANA ARBOLEYA-ARBOLEYA[2], AND FERNANDO LAS-HERAS[1], (Senior Member, IEEE)

[1]Department Ingeniería Eléctrica, Universidad de Oviedo, 33203 Gijón, Spain
[2]Epoc Polytech'laboratory, Université Nice Sophia-Antipolis, 06940 Alpes Maritimes, France

Corresponding author: Jaime Laviada (jlaviada@tsc.uniovi.es)

This work was supported in part by the Ministerio de Ciencia e Innovación of Spain /FEDER under Project TEC2014-55290-JIN and Project TEC2014-54005-P, in part by the Gobierno del Principado de Asturias (PCTI)/FEDER-FSE under Project GRUPIN14-114, and in part by the Ayudas Fundación BBVA a Investigadores y Creadores Culturales 2016.

ABSTRACT The aim of this paper is to introduce the use of sparse multistatic arrays to reduce the number of elements in novel portable and muti-view millimiter-wave scanners. Thus, the complexity of these novel scanners is significantly reduced. Furthermore, sparsity is expected to enable embedding a conventional optical camera sensor inside the aperture of the scanner allowing a reduction of the scanner size. This camera sensor is used to build a complementary 3-D optical model as well as to estimate the millimeter-wave scanner position so that the imaging merging techniques can be applied. The approach is validated for concealed weapon detection by means of simulation as well as measurements, in which the scanner aperture is emulated by raster scan, showing a performance comparable to the case of dense arrays.

INDEX TERMS Millimeter-wave imaging, mm-wave, portable camera, multiview imaging, structure from motion.

I. INTRODUCTION

Electromagnetic imaging enables the construction of images resembling real-life images by acquiring the field radiated or scattered by a given target. In contrast to conventional images, which are also assembled from electromagnetic (EM) waves but at the visible spectrum, EM imaging, which usually refers to images built from microwaves, millimeter-(mm-) or submillimeter-waves (submm-waves), is able to provide insightful information thanks to the penetration capabilities of this kind of waves. This characteristic is improved by considering low frequency ranges at the expenses of image resolution as the latter proportional to the wavelength.

In particular, mm-wave imaging provides a fair trade-off between penetration capabilities and resolution, which has become appealing for many fields such as non-destructive evaluation [1], [2], food inspection [3], concealed-weapon detection [4] or automotive radars [5]. Furthermore, the high available bandwidth make them appealing also for the broadband wireless communications [6] industry. Consequently, this technology has experimented a high boost in the last years and the cost of the components has become highly competitive.

Thus, the aforementioned features of mm-wave imaging and the cost reduction of developing this technology are expected to provide a wide variety of portable scanners, some already available [7] similar to the ones recently developed at microwaves [8], [9] or submm-waves [10].

A problem common to most of these EM scanners is that they are only able to acquire and process data from a single point of view and, therefore, they cannot provide information for an entire three-dimensional (3D) model. This problem has been recently considered by several authors [11], [12] in the field of concealed weapon detection as the capability of a global scan can provide a much more valuable information compared to a local scan. However, current approaches assume that the position of the transmitters/receivers is known *a priori* in order to fuse data. Consequently, the application to portable scanners, which could be moved along arbitrary trajectories, is not straightforward.

In the context of imaging from visible spectrum pictures, it is well-known that conventional optical cameras have been able to produce models containing information from multiple angles by resorting to approaches such as stereoscopic vision [13] or structure from motion (SfM) [14] that are

able to merge the information from different views to yield a global model. Furthermore, these techniques can run on real-time, even on affordable smartphones [15], enabling a dynamic 3D scanning.

The concept of a multi-view portable mm-wave scanners, exploiting the aforementioned advantages of optical scanners, has been recently proposed with very promising results [16]. Nevertheless, the approach was based on conventional Synthetic Aperture Radar (SAR) techniques and, therefore, it requires a dense aperture. In the last years, the use of sparse multistatic radars, also known as multiple input multiple output (MIMO) radars, has been applied for concealed weapon detection [17] enabling a strong reduction of the number of required transmitters and receivers. This reduction is achieved by arranging elements so that they result in a dense *array equivalent aperture*, a concept that has been widely exploited in acoustics [18], [19]. Furthermore, the use of *ad-hoc* postprocessing techniques enables the efficient generation of images [20], [21].

The contribution of this paper is the introduction and validation of sparse multistatic layouts for portable multi-view scanners. This results in a strong reduction of the complexity of the device. Furthermore, the optical camera, required for the positioning system, can be easily embedded inside the scanner aperture without the need of introducing an offset [16]. Results are validated by means of realistic simulations as well as measurements for one and two-dimensional (2D) effective apertures for concealed weapon detection applications.

The remaining of this paper is structured as follows. Section II is devoted to present the major concepts involved in the paper: 1) a summary of the concepts involved in the operation of the multi-view scanners; 2) the proposed multistatic layout and image processing; 3) the evaluation of the image quality achieved by different transmitter/receiver (TX/RX) arrangements. Next section, presents a validation of the technique by means of a simulation example. The technique is also validated by two measurement setups that simulate the scanner aperture by raster scanning. Finally, conclusions are drawn.

II. MULTIVIEW IMAGING WITH MULTISTATIC MM-WAVE ARRAYS

A. PORTABLE MULTIVIEW SCANNER

Multi-view mm-wave imaging was presented in [16] in parallel with the concept of stereoscopic or SfM techniques, which are able to form a 3D image from different conventional (i.e., optical) pictures. Similar to the results presented in [15] for a smartphone equipped with a camera, a portable mm-wave scanner, also equipped with a camera, is moved around a given target. Several mm-wave and optical pictures acquisitions are synchronously performed.

Conventional pictures are processed by standard SfM techniques with a two-fold purpose. First, they dynamically provide a 3D model of the body under test. Second, the position and pose of the scanner are also estimated from the pictures. Consequently, a set of rotation matrices and position vectors are obtained on-the-fly.

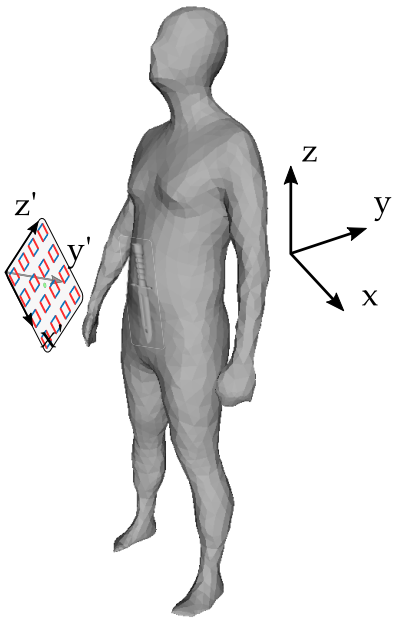

Fig. 1. Global and local systems of coordinates for a given view of the scanner.

On the other hand, mm-wave acquisitions are synchronously performed by sequentially activating a grid of dense transceivers at different discrete frequencies. The acquired scattered data is processed to estimate the reflectivity on local areas in front of the current scanner position. This reflectivity, can be used to form images resembling conventional images but with the capability to pass through some materials [4]. In particular, each local reflectivity ρ_n, obtained for the n-th acquisition position, is given by standard matched filter techniques [22]:

$$\rho_n(\vec{r}) = \sum_{p=1}^{N_f} \sum_{n=1}^{N_{trx}} s(\vec{r}_n, k_p)\, e^{j2k_p \|\vec{r}-\vec{r}_n\|_2} \tag{1}$$

where $\vec{r}$ is the observation point, $s(\vec{r}_n, k_p)$ is the scattered field, acquired by the n-th transceiver at the p-th frequency, $\vec{r}_n$ is the position of the n-th transceiver, k_p is the corresponding wavenumber at the p-th frequency, N_f is the number of considered frequencies and N_{trx} is the number of transceivers.

In general, the local coordinate system of the scanner will not be aligned with the global system of coordinates and, therefore, the reflectivity is usually computed for the local system of coordinates for the n-th position (see Fig. 1). In practice, (1) is expressed in terms of Fourier transforms by introducing the stationary phase method so that a fast evaluation can be performed [4], [22].

Each new computed local reflectivity for the n-th position is translated to the global system of coordinates by means of

the corresponding rotation matrix and translation vector and, after that, merged to construct a global reflectivity $\rho_{g,n}$ by means of the following iterative formulation [16]:

$$\rho_{g,n}(\vec{r}) = \max\left\{\left|\rho_{g,n-1}(\vec{r})\right|, \left|\rho_n(\vec{r})\right|\right\}. \quad (2)$$

Thus, a mm-wave and optical model, referred to the same system of coordinates, are built on-the-fly.

B. SPARSE MULTISTATIC LAYOUT

In contrast to standard synthetic aperture imaging with a grid of dense transceivers [4], if the TX and RX elements are separated, a more efficient approach, in terms of number of elements, can be obtained. In this case, it is possible to prove that, in the far-field, this setup is equivalent to an aperture with a distribution given by the convolution of the TXs and RXs [19]:

$$a_{eff} = a_t * a_r \quad (3)$$

where a_{eff} is usually referred to as array effective aperture and a_t and a_r are the TX and RX apertures, respectively. Consequently, it is possible to design a sparse array so that its corresponding equivalent aperture is dense and, therefore, it lacks of grating lobes despite of the sparsity in the real aperture. Furthermore, depending on the design, the effective aperture will be tapered resulting in lower secondary side lobes.

In the case of multistatic layouts, the reflectivity can also be computed by means of a matched filter [23] as:

$$\rho_n(\vec{r}) = \sum_{n=1}^{N_{tx}} \sum_{m=1}^{N_{rx}} \sum_{p=1}^{N_f} s(\vec{r}_{tx,n}, \vec{r}_{rx,m}, k_p) \, e^{jk_p \|\vec{r}-\vec{r}_{tx,n}\|_2} e^{jk_p \|\vec{r}-\vec{r}_{rx,p}\|_2} \quad (4)$$

where $s(\vec{r}_{tx,n}, \vec{r}_{rx,m}, k_p)$ is the scattered field at the p-th frequency f_p when the active TX/RX pair, formed by the n-th TX located at $\vec{r}_{tx,n}$ and the m-th RX located at $\vec{r}_{rx,n}$, is active; N_{tx}, N_{rx} and N_f are the number of TXs, RXs and frequencies, respectively; and, k_p is the wavenumber at the p-th frequency.

In a similar fashion to the monostatic case, an efficient formulation can be also achieved by resorting to the stationary phase approximation [20], [23] or correction factors converting MIMO data to conventional monostatic data [21] so that the evaluation of (4) can be performed by means of Fast Fourier transforms.

C. EVALUATION OF DIFFERENT SPARSE TOPOLOGIES

Although the effective aperture concept is only valid for the far-field, it is also employed for the design of near-field imaging systems as there are no guidelines for the design in the near-field [23]. This fact is specially relevant for scanners operating at short distances such as the proposed portable scanners. Thus, the evaluation of two sparse multistatic layouts and the comparison with a dense monostatic setup is considered in this section.

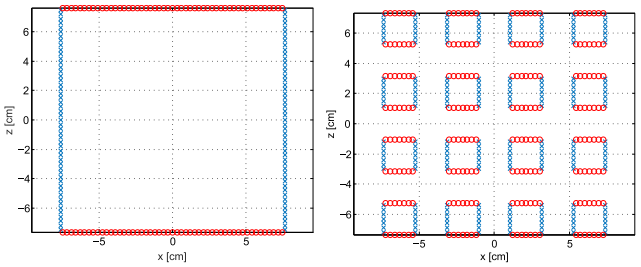

Fig. 2. Considered multistatic topologies: a) Multistatic setup with a single cluster; b) Multistatic setup with 4 × 4 clusters. TXs and RXs are denoted by blue crosses and red circles, respectively.

TABLE 1. Comparison of point spread functions characteristics at 30 cm from the array aperture. Mult. 1 × 1 refers to the setup with a single cluster whereas Mult. 4 × 4 referres to the 4 × 4 setup.

Method	δ_l	δ_d	SLL
Monostatic	3.5 mm	25.5 mm	−12.8 dB
Mult. 1x1	3.5 mm	31.0 mm	−13.2 dB
Mult. 4x4	4.6 mm	27.8 mm	−23.5 dB

The multistatic topologies are shown in Fig. 2. The first multistatic layout (see Fig. 2(a)) consists of a single cluster of TXs and RXs along a 15.3 cm × 15.3 cm aperture with a spacing of 3 mm between adjacent elements. Thus, this architecture involves 102 TXs and 102 RXs (i.e., the total number of elements is 204). According to (3), this layout results in an aperture without any taper.

The second considered multistatic array, shown in Fig. 2(b), is a reduced version of the one presented in [17] fitting in an area of 14.7 cm × 14.7 cm. This topology involves 4 × 4 clusters separated by 2.1 cm. The separation between consecutive TXs or RXs inside a given cluster is 3 mm as in the previous example. In this case, the number of TXs and RXs is 224 in both cases (i.e., 448 total elements). In contrast to the previous case, this kind of arrangement results in a tapered aperture according to (3). It is worth mentioning that both layouts have space enough to embed an optical camera inside them.

Finally, the monostatic aperture consists of a grid of 80 × 80 transceivers (i.e., 6400 total elements) along an area of 15 cm × 15 cm. Thus, the spacing between elements is 1.9 mm, which is *a priori* advantageous compared to the considered sparse multistatic topologies.

In all the cases considered in this section, the frequency range is set from 75 GHz to 79 GHz with a total of 24 equally spaced frequency points.

Results for the point spread function (PSF) in case of a target at 30 cm from the aperture are summarized in Table 1 in terms of lateral resolution δ_l, depth resolution δ_d and lateral side lobe level (SLL).. In addition, PSF cuts are shown in Fig. 3.

It is interesting to note that the lateral resolution is similar for the monostatic and single cluster architectures as they correspond to non-tapered apertures. Nevertheless, they result in

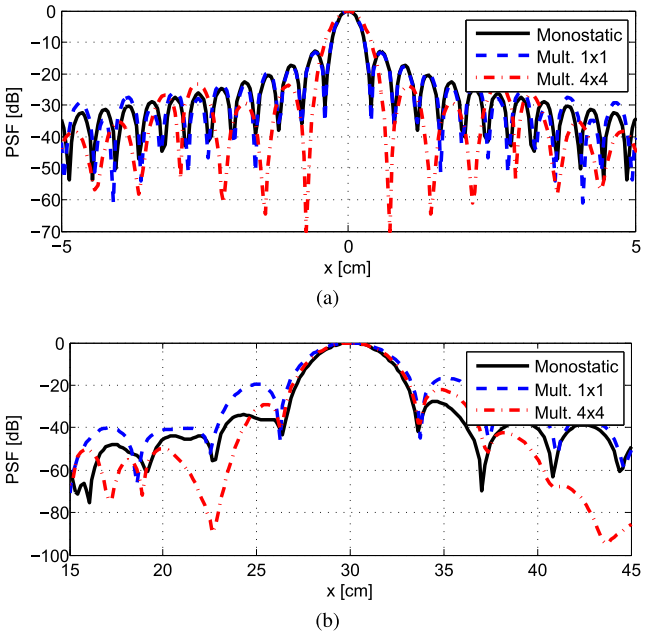

Fig. 3. PSF cuts: (a) lateral cut; (b) depth cut.

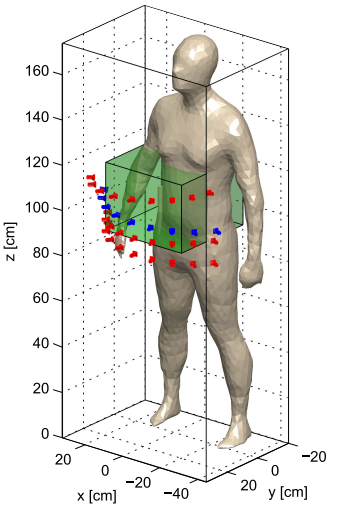

Fig. 4. Human model with attached knife. Cameras considered for the different examples and the reconstruction volume are also shown. Cameras highlighted in blue are used to obtain the results in Fig. 5 whereas all the cameras (red and blue colored) are used in the rest of the examples.

SLL of (approximately) -13 dB as it is expected for a flat aperture. On the other hand, the 4×4 cluster version results in a significant reduction of the SLL at the expenses of losing some lateral resolution.

Fig. 5 shows a comparison of reflectivity cut at $z = 100$ cm for the model shown in Fig. 4 of a human being with an attached knife. Only the 9 blue-highlighted positions, located around the considered z plane, were used in this example. The impact of the secondary lobes becomes clear in this example as the version with the 4×4 arrangement is mostly free of strange artifacts revealing the cleanest profile in which the handle of the knife is visible.

III. RESULTS

In this section, several simulation and measurements are shown to illustrate the proposed approach. Since the reflectivities are, in general, evaluated in a 3D space, several possibilities can be taken into account to represent them. In this paper, the same approach as in [16], where a surface $s(x, z)$ is constructed by projecting the 3D reflectivity along one axis, is used as follows:

$$s(x, z) = \arg\max_{y} |\rho(x, y, z)| \tag{5}$$

where the y-axis has been considered for the projection in this case. Furthermore, this surface is colored according to the depth along the projection axis and the brightness of each pixel is weighted by the reflectivity value in a similar fashion to [17].

A. SIMULATION RESULTS

In this first example, a simulation of the multistatic system is performed. A multistatic aperture, limited to a maximum dimension of 16 cm is considered. In particular, the arrangement shown in Fig. 2(b) is used. The radiation pattern of all the elements is modeled by means of a $\cos^q$ radiation pattern with $q = 1$ [24].

The scanner aperture is moved along 36 positions around a human body torso with an attached knife as shown in Fig. 4. For each TX/RX pair, the frequency sweep consists of 24 points equally spaced from 75 GHz to 79 GHz. In order to alleviate the simulation cost, the problem is simulated by means of Feko using the optical physics solver for electrically large triangles.

The reflectivity is calculated in the cuboid shown in Fig. 4 with ranges of $[-20\,\text{cm}, 20\,\text{cm}]$, $[-20\,\text{cm}, 20\,\text{cm}]$ and $[90\,\text{cm}, 120\,\text{cm}]$ for the x-, y- and z-axis, respectively. These cuboid is discretized with an step of 3.8 mm for all the axes. Since this step is smaller than the resolutions reported in Table. 1, the obtained resolution is not expected to be degraded by this step choice.

The cumulative results for different numbers of positions are reported in Fig. 6 and the final imaging results are shown in Fig. 7. In this example, the handle and blade of the knife can be easily detected by simple inspection. It is interesting to observe that the handle in the mm-wave image is found to be significantly larger than the real one. Due to the circular geometry of this part, specular reflection can be found for multiple views and, therefore, the object is limited by the depth resolution given in Table 1.

In contrast, the blade does not suffer from this distortion as specular reflection is only found when the scanner is almost normal to the blade, i.e., parallel to the xz-plane. Consequently, the depth resolution is not perceived in the considered projection and the image is only limited by the lateral resolution.

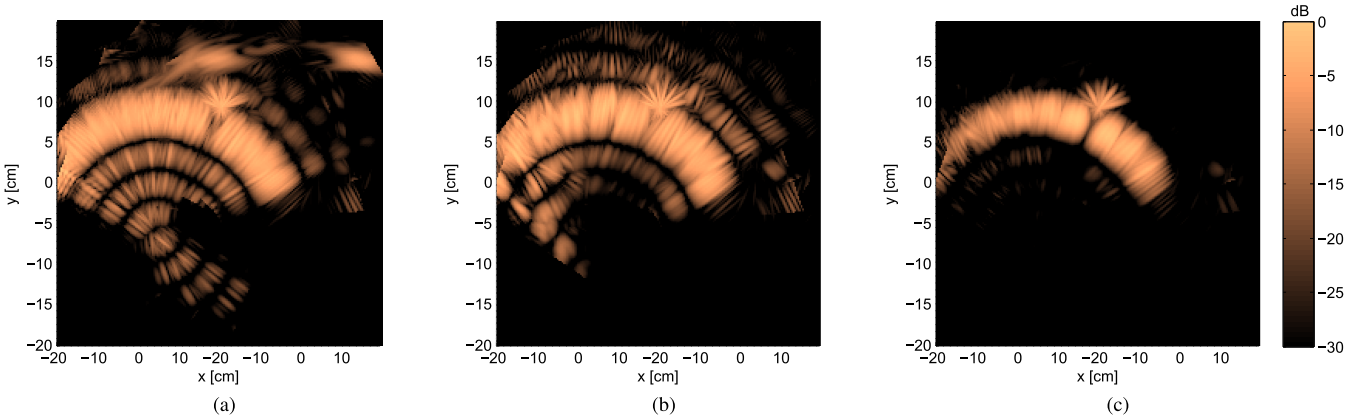

Fig. 5. Comparison of a reflectivity cut normalized to the maximum: a) Monostatic setup; b) Multistatic setup with a single cluster; c) Multistatic setup with a 4 × 4 cluster arrangement.

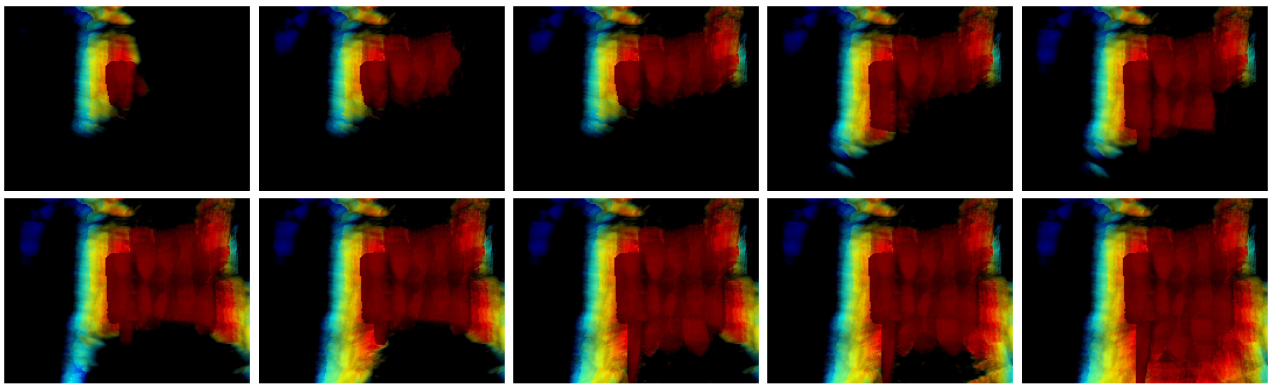

Fig. 6. Partial results for the cumulative reflectivity in the simulation example described in Fig. 4. Results (from left to right and up to down) corresponds to 3, 6, 9, 12, 15, 19, 21, 24, 29 and 36 scanner positions.

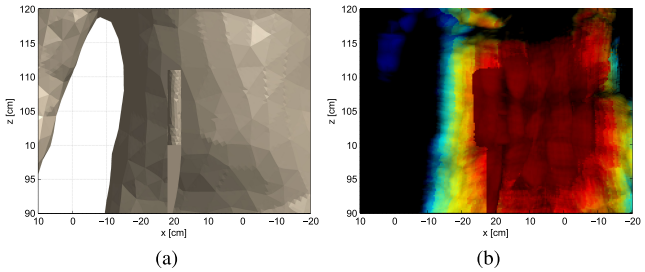

Fig. 7. Detail of the area with the attached knife: a) simulated model; b) mm-wave image.

B. ONE-DIMENSIONAL APERTURE MEASUREMENT

In order to validate the performance of the proposed approach with measurements, a first example with a one-dimensional (1D) aperture along x is considered (see Fig. 8). Consequently, this topology cannot provide resolution along the z-axis.

This scanner aperture is emulated by raster scanning with two frequency extension modules mounted on linear stages. Thus, the TX module was mounted on a linear positioner whereas the RX was mounted on a multi-axis positioner with 3D movement capacity (see Fig. 9). Nevertheless, the movements of the later positioner were limited to a single dimension in this example.

The number of TXs is set to eight and they are equally spaced 19.5 mm. The RXs are arranged into four clusters separated 2.1 cm. Each group comprises 13 RXs equally spaced 1.5 mm. It is straightforward to prove that this distribution results in an effective aperture with equally spaced elements as given by (3). Due to the physical size of the general purpose mm-wave modules, a separation of 11.5 cm was set between the TX and RX baselines.

A mannequin torso covered by aluminum foil to mimic the skin reflectivity is considered. In addition, a metallic bar with 2 cm section is attached to the torso to model a protrusion (see Fig. 9(a)). The dressed mannequin is mounted on a rotary platform so that a setup equivalent to moving the aperture around the mannequin is achieved (see Fig. 9(b)).

A smartphone equipped with a conventional camera is placed at 5.5 cm over the RX module aperture (i.e., along the scanner local z-axis) to automatically take pictures of the targets from the different views. A second displacement of -9 cm along the local y-axis had to be introduced due to physical constraints when implementing the setup. Both

TABLE 2. Real and estimated positions for the 1D aperture measurement example. Attitudes are also provided as yaw (γ), pitch (α) and roll (β). The $\hat{}$ is used to denote estimation.

Scanner position						Scanner attitude					
x [cm]	$\hat{x}$ [cm]	y [cm]	$\hat{y}$ [cm]	z [cm]	$\hat{z}$ [cm]	γ [deg.]	$\hat{\gamma}$ [deg.]	α [deg.]	$\hat{\alpha}$ [deg.]	β [deg.]	$\hat{\beta}$ [deg.]
11.80	14.31	32.42	31.97	0	0.1	20	21.69	0	0.11	0	-0.05
6.00	7.34	33.98	33.88	0	0.1	10	11.02	0	0.10	0	-0.02
0	0.00	34.50	34.50	0	0.0	0	0	0	0.00	0	0.00
-6.00	-7.18	33.98	33.75	0	-0.1	-10	-10.62	0	-0.13	0	0.01
-11.80	-13.83	32.42	31.73	0	0.1	-20	-20.66	0	0.09	0	0.06

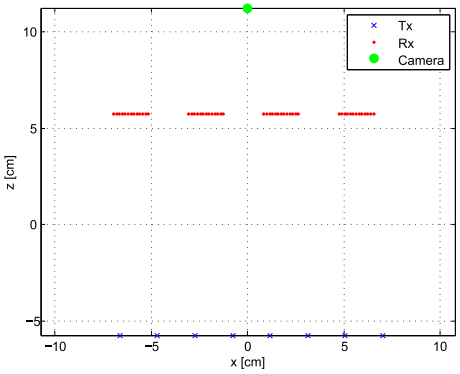

Fig. 8. TX and RX positions for the 1D aperture measurement example.

(a) (b)

Fig. 9. One-dimensional aperture measurement example: a) mannequin with attached bar; b) dressed mannequin.

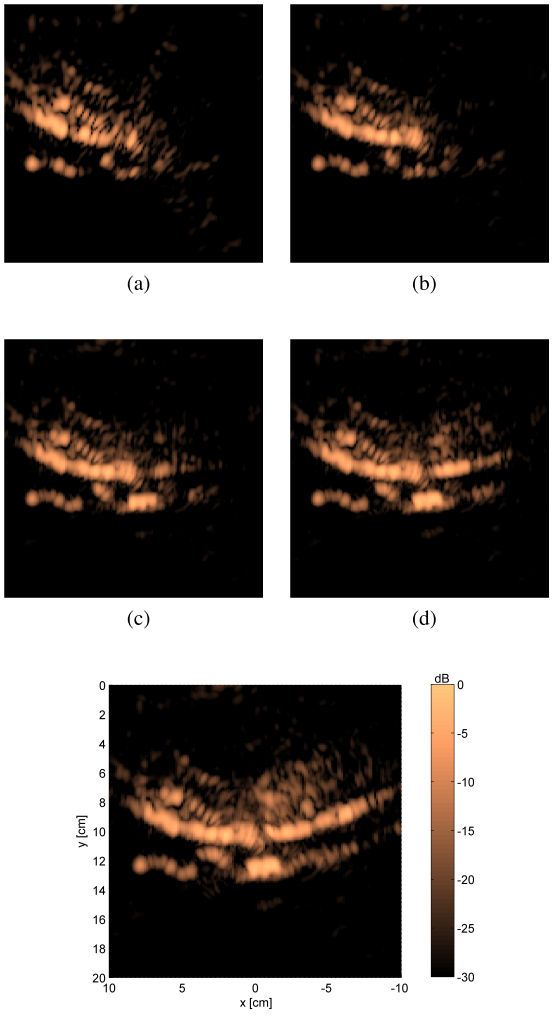

(a) (b) (c) (d) (e)

Fig. 10. Cumulative reflectivity for the 1D aperture example. Results are normalized with respect to the maximum value.

displacements were corrected during the data postprocessing to correctly estimate the position of the scanner aperture and the offset between the mm-wave and the optical models by means of standard translation and rotation operations.

The mm-wave data were acquired at 5 different angular positions for the frequency range from 75 GHz to 110 GHz sampled with 401 equally spaced frequency points. A Hamming window was applied to each frequency sweep to reduce the secondary side lobe level in the down-range direction.

The angular increment between different views with the mm-wave scanning system was 10°. Nevertheless, the conventional optical camera pictures were taken with an angular step of 5° so that they were taken from the same views as the mm-wave acquisitions plus four intermediate acquisitions to increase the degree of overlap. Finally, 3 additional pictures were taken with an step of 1 cm to calibrate the scale of the computed model. The optical data were processed by SfM software [14], [25] to estimate the positions.

In order to compare the estimated positions and the theoretical ones, the central acquisition point was translated to the central theoretical point. In addition, the estimated

TABLE 3. Real and estimated positions for the 2D aperture measurement. Attitudes are also provided as yaw (γ), pitch (α) and roll (β). The $\hat{}$ is used to denote estimation.

Scanner position						Scanner attitude					
x [cm]	$\hat{x}$ [cm]	y [cm]	$\hat{y}$ [cm]	z [cm]	$\hat{z}$ [cm]	γ [deg.]	$\hat{\gamma}$ [deg.]	α [deg.]	$\hat{\alpha}$ [deg.]	β [deg.]	$\hat{\beta}$ [deg.]
11.8	12.1	32.4	31.89	0	0.0	20	19.7	0	0.07	0	-0.2
6.0	6.1	34.0	33.71	0	0.0	10	9.8	0	0.01	0	-0.1
0	0.0	34.5	34.50	0	0.0	0	0	0	0.00	0	0
-6.0	-6.3	34.0	34.20	0	0.0	-10	-9.8	0	0.03	0	0.1
-11.8	-12.5	32.4	32.83	0	0.0	-20	-19.7	0	0.01	0	0.2

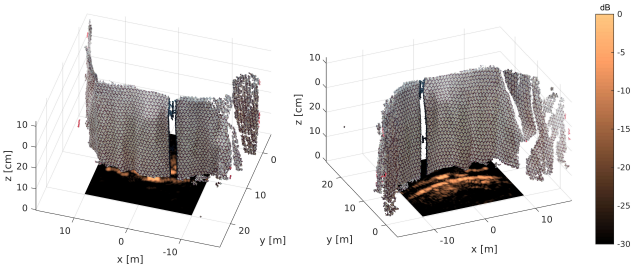

Fig. 11. Dense point cloud and reflectivity for the 1D aperture example: (a) front view; (b) rear view.

(a) (b)

Fig. 12. Multiview measurement setup for a knife attached to a mannequin torso covered by aluminum foil: a) undressed; b) dressed.

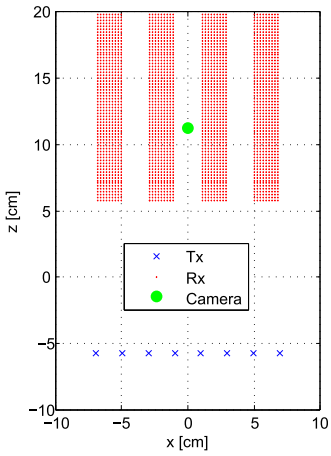

Fig. 13. TX and RX positions for the 2D aperture measurement example.

points were rotated so that the pointing vector of the central point points towards $-\hat{y}$ with the aperture parallel to the xz plane and the baseline parallel to the global x-axis. Table 2 shows these theoretical and estimated positions with a very good agreement. It is relevant to note that despite absolute positioning has a centimeter error, which could be considered as high for the expected lateral resolutions in the order of a few millimeters, the relative error between adjacent positions (i.e., the displacement between adjacent positions) is in the order of a few millimeters and, consequently, it does not significantly degrade the resolution provided by the mm-wave imaging.

Fig. 10 shows the cumulative reconstruction after considering each mm-wave acquisition. The torso profile can be easily perceived with a protrusion corresponding to the metallic bar. Although no imaging artifacts appear along the profile, a significant clutter can be found behind the torso profile due to the lack of vertical resolution.

The dense point cloud from the optical model and the mm-wave model are both superposed in Fig. 11. A detailed inspection reveals that the metallic bar fits in the dress wrinkle showing good agreement between both models.

C. TWO-DIMENSIONAL APERTURE MEASUREMENT

Once the correct working of the approach has been checked for a 1D aperture, the approach is validated for a two-dimensional (2D) aperture, which is expected to provide results similar to the ones of a final scanner. For this purpose, the setup shown in Fig. 12 is considered. In this setup, the target under test is the same mannequin torso covered by aluminum foil but with an attached knife (see Fig. 12(a)).

The aperture is emulated by means of a double raster scan. In particular, a general purpose RX mm-wave extension module is mounted on a three-axes positioner so that it is moved along the RX positions. On the other hand, a TX module is mounted on a linear micropositioner stage in order to cover the TX positions (see Fig. 12).

However, due to the physical restriction related to the size of the general purpose mm-wave modules, the considered topology must guarantee a minimum distance between the TX and RX. Since the TX module was mounted on a linear micropositioner, its movement was limited to the x-axis. Consequently, a dense effective aperture was achieved by using a hybrid sampling along the RX positions. Thus, a sparse

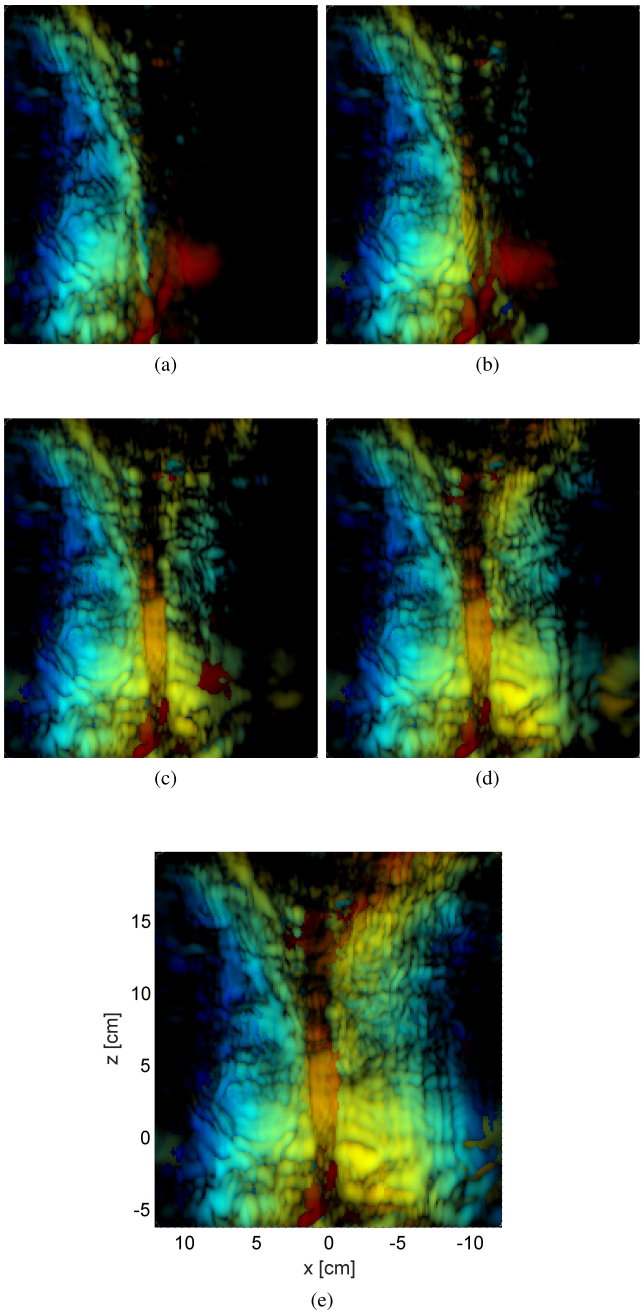

Fig. 14. Cumulative reflectivity for the three-dimensional example for different number of scanner acquisitions: a) one; b) two; c) three; d) four; e) five.

sampling was used along the x-axis whereas a dense sampling was used along the z-axis.

The considered TX and RX positions are shown in Fig. 13. Thus, eight TXs are equally spaced 19.8 mm along the x-axis. On the other hand, the RXs are arranged into four equal groups, separated by 2.2 cm. Each group comprises a grid of 9×260 elements with an spacing in both directions of 2.2 mm. The distance between the RX an TX baselines is 115 mm.

As in the previous example, the considered frequency range is 75 GHz-110 GHz with 401 frequency steps.

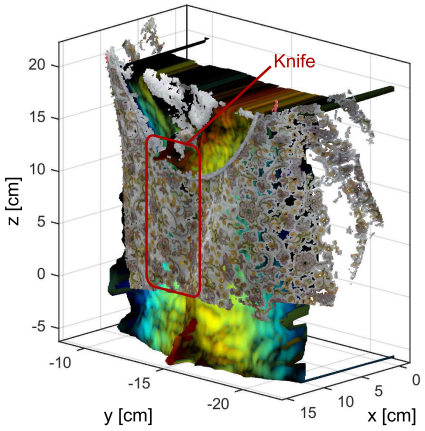

Fig. 15. 3D mm-wave model with a dense point cloud overlay for the 2D aperture measurement.

The movement of the scanner around the target under test is again achieved by rotating the mannequin torso so that data from different points of view can be acquired. The distance from the plane containing the scanner aperture to the rotation axis is 34.5 cm resulting in a distance in the order of approximately 22 cm to the mannequin torso (this distance depends on the rotation angle).

The scanner positions are estimated from the pictures taken by a camera mounted on the RX module. After the mm-wave data acquisition for each scanner position, the RX positioner is moved to the center of the baseline ($x = 0$ cm and $z = 5.75$ cm, according to the system of coordinates in Fig. 13) and a picture is taken. Due to the same physical restrictions encountered in the previous example, the camera is mounted with an offset of $z_{off} = 5.5$ cm and $y_{off} = -9$ cm.

As in the previous example, the target is rotated with increments of 10° but pictures are also taken at intermediate points. The system was also calibrated with 3 extra images taken with a known displacement of 1 cm. The real and estimated mm-wave scanner positions are gathered in Table 3, revealing a very good agreement. It is important to observe that the accuracy error is in the order of the lateral and depth resolutions of the scanner.

The system of coordinates was chosen as in the previous case so that the central points meets the theoretical one and the scanner at the central position points towards $\hat{y}$ with the TX baseline parallel to the xz plane. In addition, the origin of coordinates was set at an arbitrary height along the center of rotation which is defined as $z = 0$. The reflectivity was computed on an cuboid ranging from -12 cm to 12 cm in the x-axis, from 10 cm to 20 cm in the y-axis and from -17.75 cm to 8.25 cm in the z-axis. The number of points for each axis was 201, 101 and 241, respectively, resulting in a step of approximately 1 mm.

The cumulative imaging results for the five positions are shown in Fig. 14. After considering all the positions, which are centered around the middle of the knife, the central area of the knife, including the upper part of the blade and the

lower part of the handle, can be clearly seen. As shown in the simulation result and in [16] for dense apertures, the rest of the knife could be imaged by considering additional positions above and below the already considered ones.

Fig. 15 shows the 3D mm-wave together with the dense point cloud calculated by SfM with an excellent agreement between both models.

IV. CONCLUSIONS

Multistatic topologies for multi-view imaging have been proved to exhibit advantages similar to the ones already observed for large scanners. In particular, they exhibit a less dense aperture that can greatly reduce the weight of portable devices as well as the overall cost. Moreover, the sparsity can be exploited to include the required optical camera inside the aperture, reducing the total size of the scanner.

Depending on the chosen layout, the aperture can be equivalent to a tapered aperture which provides a lower side lobe level at the expense of a reduction of the lateral resolution.

The obtained results shows that the imaging capabilities are similar to the ones obtained by a dense standard aperture. In particular, the approach has been validated in the field of concealed weapon detection exhibiting good capabilities to find dangerous objects under clothing with arrays with an aperture of approximately 15 cm.

REFERENCES

[1] S. Kharkovsky, J. T. Case, M. A. Abou-Khousa, R. Zoughi, and F. L. Hepburn, "Millimeter-wave detection of localized anomalies in the space shuttle external fuel tank insulating foam," *IEEE Trans. Instrum. Meas.*, vol. 55, no. 4, pp. 1250–1257, Aug. 2006.

[2] S. Kharkovsky and R. Zoughi, "Microwave and millimeter wave nondestructive testing and evaluation—Overview and recent advances," *IEEE Instrum. Meas. Mag.*, vol. 10, no. 2, pp. 26–38, Apr. 2007.

[3] G. Ok, K. Park, H. S. Chun, H.-J. Chang, N. Lee, and S.-W. Choi, "High-performance sub-terahertz transmission imaging system for food inspection," *Biomed. Opt. Exp.*, vol. 6, no. 5, pp. 1929–1941, 2015.

[4] D. M. Sheen, D. L. McMakin, and T. E. Hall, "Three-dimensional millimeter-wave imaging for concealed weapon detection," *IEEE Trans. Microw. Theory Techn.*, vol. 49, no. 9, pp. 1581–1592, Sep. 2001.

[5] H. Knapp *et al.*, "SiGe circuits for automotive radar," in *Proc. Topical Meet. Silicon Monolithic Integr. Circuits RF Syst.*, Jan. 2007, pp. 231–236.

[6] N. Dolatsha *et al.*, "A compact 130 GHz fully packaged point-to-point wireless system with 3D-printed 26 dBi lens antenna achieving 12.5 Gb/s at 1.55 pJ/b/m," in *IEEE Int. Solid-State Circuits Conf. (ISSCC) Dig. Tech. Papers*, Feb. 2017, pp. 306–307.

[7] M. Klenner *et al.*, "A portable W-band radar system for enhancement of infrared vision in fire fighting operations," *Proc. SPIE*, vol. 9993, pp. 26–29, Sep. 2016.

[8] M. T. Ghasr, M. A. Abou-Khousa, S. Kharkovsky, R. Zoughi, and D. Pommerenke, "Portable real-time microwave camera at 24 GHz," *IEEE Trans. Antennas Propag.*, vol. 60, no. 2, pp. 1114–1125, Feb. 2012.

[9] M. T. Ghasr, M. J. Horst, M. R. Dvorsky, and R. Zoughi, "Wideband microwave camera for real-time 3-D imaging," *IEEE Trans. Antennas Propag.*, vol. 65, no. 1, pp. 258–268, Jan. 2017.

[10] H. Sherry *et al.*, "A 1 kpixel CMOS camera chip for 25 fps real-time terahertz imaging applications," in *IEEE Int. Solid-State Circuits Conf. (ISSCC) Dig. Tech. Papers*, Feb. 2012, pp. 252–254.

[11] F. Gumbmann and S. S. Ahmed, "Novel walk-through imaging system for security screening," SPIE Newsroom, Nov. 2016. [Online]. Avaliable: http://spie.org/newsroom/6703-novel-walk-through-imaging-system-for-security-screening?SSO=1, doi: 10.1117/2.1201609.006703.

[12] B. González-Valdés, Y. Álvarez, S. Mantzavinos, C. M. Rappaport, F. Las-Heras, and J. A. Martinez-Lorenzo, "Improving security screening: A comparison of multistatic radar configurations for human body imaging," *IEEE Antennas Propag. Mag.*, vol. 58, no. 4, pp. 35–47, Aug. 2016.

[13] R. Hartley and A. Zisserman, *Multiple View Geometry in Computer Vision*. Cambridge, U.K.: Cambridge Univ. Press, 2003.

[14] C. Wu, "Towards linear-time incremental structure from motion," in *Proc. Int. Conf. 3DTV*, Seattle, WA, USA, Jun./Jul. 2013, pp. 127–134.

[15] P. Tanskanen, K. Kolev, L. Meier, F. Camposeco, O. Saurer, and M. Pollefeys, "Live metric 3D reconstruction on mobile phones," in *Proc. Int. Conf. Comput. Vis. (ICCV)*, Sydney, NSW, Australia, Dec. 2013, pp. 65–72.

[16] J. Laviada, A. Arboleya-Arboleya, Y. Álvarez, B. González-Valdés, and F. Las-Heras, "Multiview three-dimensional reconstruction by millimetre-wave portable camera," *Sci. Rep.*, vol. 7, Jul. 2017, Art. no. 6479.

[17] S. S. Ahmed, A. Schiessl, and L.-P. Schmidt, "A novel fully electronic active real-time imager based on a planar multistatic sparse array," *IEEE Trans. Microw. Theory Techn.*, vol. 59, no. 12, pp. 3567–3576, Dec. 2011.

[18] S. W. Smith, H. G. Pavy, and O. T. von Ramm, "High-speed ultrasound volumetric imaging system. I. Transducer design and beam steering," *IEEE Trans. Ultrason., Ferroelect., Freq. Control*, vol. 38, no. 2, pp. 100–108, Mar. 1991.

[19] G. R. Lockwood and F. S. Foster, "Optimizing sparse two-dimensional transducer arrays using an effective aperture approach," in *Proc. IEEE Ultrason. Symp.*, vol. 3. Oct. 1994, pp. 1497–1501.

[20] X. Zhuge and A. G. Yarovoy, "Three-dimensional near-field MIMO array imaging using range migration techniques," *IEEE Trans. Image Process.*, vol. 21, no. 6, pp. 3026–3033, Jun. 2012.

[21] H. Nguyen, D. Maurais-Galejs, T. Anderson, J. Krieger, W. Moulder, and J. Muldavin, "Scalable prototyping testbed for MMW imager system," in *Proc. IEEE Int. Symp. Phased Array Syst. Technol. (PAST)*, Oct. 2016, pp. 1–6.

[22] J. M. Lopez-Sanchez and J. Fortuny-Guasch, "3-D radar imaging using range migration techniques," *IEEE Trans. Antennas Propag.*, vol. 48, no. 5, pp. 728–737, May 2000.

[23] S. S. Ahmed, *Electronic Microwave Imaging With Planar Multistatic Arrays*. Berlin, Germany: Logos Verlag, 2014.

[24] Y. T. Lo and S. W. Lee, Eds., *Antenna Handbook: Antenna Fundamentals and Mathematical Techniques*. New York, NY, USA: Van Nostrand, 1993.

[25] C. Wu. (2011). *VisualSFM: A Visual Structure From Motion System*. [Online]. Available: http://ccwu.me/vsfm/

JAIME LAVIADA was born in Gijón, Spain. He received the M.S. degree in telecommunication engineering and the Ph.D. degree from the Universidad de Oviedo, Spain, in 2005 and 2010, respectively. In 2006, he joined the Research Group Signal Theory and Communications, Universidad de Oviedo, where he was involved in multiple national and European projects and contracts with several companies. In 2015, he was with the Antennas Group, Universidad Pública de Navarra with a National Postdoctoral Fellowship collaborating in several applied research projects. He is currently with the Universidad de Oviedo, where he currently holds an assistant professor position. From 2007 to 2008, he was a Visiting Scholar with the Electromagnetics and Communications Laboratory, Pennsylvania State University. He is currently with the Applied Microwave Non-Destructive Testing Laboratory, Missouri Science and Technology.

His research interests include numerical techniques applied to electromagnetic imaging, antenna measurements, method of moments, and antenna pattern synthesis.

ANA ARBOLEYA-ARBOLEYA received the M.Sc. and Ph.D. degrees in telecommunication engineering from the University of Oviedo, Spain, in 2009 and 2016, respectively. From 2008 to 2016, she was a Research Assistant within the Signal Theory and Communications Research Group, TSC-UNIOVI, Department of Electrical Engineering, University of Oviedo. She holds a post-doctoral position with the EpOC Polytech' Laboratory, Electronics for Connected Objects, University of Nice-Sophia Antipolis, France. She was a Visiting Scholar with the Department of Radio Science and Engineering and MilliLab, Aalto University, Finland, in 2014 and 2015. Her major research interests comprise antenna diagnostics and measurement systems and techniques, and high frequency imaging techniques and applications. She was a recipient of the 2017 National Awards of the Official College of Telecommunication Engineers of Spain to the Best Ph.D. Thesis on Telecommunication Engineering in the category of security and defense.

FERNANDO LAS-HERAS (M'86–SM'08) received the M.S. and Ph.D. degrees in telecommunication engineering from the Technical University of Madrid (UPM) in 1987 and 1990, respectively. He was a National Graduate Research Fellow from 1988 to 1990. He held an associate professor position with the Department of Signal, Systems and Radio communications, UPM, from 1991 to 2000. From 2003, he holds a full professor position with the University of Oviedo, where he was the Vice Dean for Telecommunication Engineering with the Technical School of Engineering, Gijón, from 2004 to 2008. Since 2001, he has been the Head of the Research Group Signal Theory and Communications TSC-UNIOVI with the Department of Electrical Engineering, University of Oviedo. He was a Visiting Lecturer with the National University of Engineering in Peru in 1996, a Visiting Researcher with Syracuse University, New York, in 2000, and a short term Visiting Lecturer with ESIGELEC in France from 2005 to 2011. He held the telefónica chair position on RF Technologies, ICTs applied to Environment and ICTs and Smartcities, University of Oviedo from 2005 to 2015. He has led and participated in a great number of research projects and has authored over 450 articles published in academic journals and proceedings of international conferences, mainly in the areas of antennas, propagation, metamaterials and inverse problems with application to antenna measurement (NF-FF, diagnostics and holography), electromagnetic imaging (security and NDT) and localization, developing computational electromagnetics algorithms and technology on microwaves, millimeter wave, and THz frequency bands. Member of the board of directors of the IEEE Spain Section from 2012 to 2015, member of the board IEEE Microwaves and Antennas Propagation Chapter (AP03/MTT17) (2016–2018) and member of the Science, Technology and Innovation Council of Asturias (2010).